The Astronomical Journal, 168:19 (12pp), 2024 July https://doi.org/10.3847/1538-3881/ad454c

The Baryonic Tully–Fisher Relation. I. WISE/Spitzer Photometry

Francis Duey[1], James Schombert[2], Stacy McGaugh[1], and Federico Lelli[3]
[1] Department of Astronomy, Case Western Reserve University, Cleveland, OH 44106, USA
[2] Department of Physics, University of Oregon, Eugene, OR 97403, USA
[3] Arcetri Astrophysical Observatory (INAF), Florence, Tuscany, Italy
Received 2023 August 31; revised 2024 April 1; accepted 2024 April 2; published 2024 June 20

Abstract

We present Wide-field Infrared Survey Explorer (WISE) W1 photometry of the Spitzer Photometry and Accurate Rotation Curves sample. The baseline of near-IR fluxes is established for use by stellar mass models, a key component to the baryonic Tully–Fisher relation and other kinematic galaxies scaling relations. We focus this paper on determination of the characteristics of the W1 fluxes compared to IRAC 3.6 μm fluxes, internal accuracy limitations from photometric techniques, external accuracy by comparison to other work in the literature and the range of W1 to IRAC 3.6 μm colors. We outline the behavior of SDSS g, W1 and IRAC 3.6 colors with respect to underlying spectral energy distribution features. We also note a previously unknown correlation between WISE colors and the central surface brightness, probably related to the low metallicity of low-surface-brightness dwarfs.

Unified Astronomy Thesaurus concepts: Galaxy structure (622); Galaxy photometry (611); Disk galaxies (391)

Supporting material: machine-readable table

1. Introduction

The classic Tully–Fisher (TF) relation links the rotation velocity of a disk galaxy to its stellar mass and/or luminosity in a given photometric band (see Kourkchi et al. 2020). Because the observed rotation velocities do not depend on galaxy distance D, while stellar luminosities depend on D^2, the TF relation has, historically, played a crucial role in constraining the value of H_o (Tully & Fisher 1977; Sakai et al. 2000). The classic TF relation, however, breaks down at stellar masses below approximately 10^9 $M_\odot$, when dwarf galaxies in groups and in the field environment become progressively more gas rich. By replacing the stellar mass with the total baryonic mass (stars plus gas, M_b), one recovers a single linear relation: the so-called baryonic Tully–Fisher relation (bTFR; Freeman 1999; McGaugh et al. 2000; Verheijen 2001; Zaritsky et al. 2014).

The bTFR samples deeper into the galaxy mass function, as low-mass dwarfs typically have high gas fractions and the neutral gas can constitute 80%–90% of the total baryonic mass (Bradford et al. 2015). This results in a large amount of scatter in the classic TF relation with a corresponding loss in accuracy as a distance indicator, which can be minimized by including the gas mass. Currently, the bTFR extends over two decades in velocity and six decades in M_b (McGaugh 2012; Iorio et al. 2017). Moreover, it displays a surprisingly small scatter, considering the number of possible competing astrophysical processes that produce this relation (Lelli et al. 2016). However, on the high baryonic mass end of the bTFR, the stellar mass of a disk galaxy dominates. Thus, while the range in the bTFR will not be dramatically increased on the high mass end compared to the low-mass end, the linearity of the bTFR is highly dependent on accurate stellar masses at the high mass end (Duey et al. 2023).

The current highest quality data to study the baryonic component of rotating galaxies is the Spitzer Photometry and Accurate Rotation Curves (SPARC) data set (Lelli et al. 2016). SPARC uses deep IR imaging to (1) determine the total stellar mass through IR photometry and (2) compute the stellar gravitation contribution to the observed rotation curve as a function of galaxy radius. The first aspect is used to derive the baryonic TF relation, the second aspect results in the new radial acceleration relation (i.e., the RAR; Lelli et al. 2017).

For stellar mass determination, the near-IR offers a portion of a galaxy's spectrum that is dominated by starlight free from strong emission lines and star-formation effects. The low Galactic and internal galactic extinction make near-IR fluxes more consistent across morphological types. In addition, an optical to near-IR color fixes a unique value for the mass-to-light ratio (Υ_*) based on stellar population models (Schombert et al. 2022) converting near-IR fluxes into stellar mass.

The SPARC project depended on pointed observations from the Spitzer Space Telescope (Werner et al. 2004). But, with the termination of the Spitzer mission, future observations will be dependent on the all-sky data set from the Wide-field Infrared Survey Explorer (WISE) mission (Wright et al. 2010). The goal of this paper is to link the photometry system of Spitzer to WISE in order to determine total IR luminosity and explore the meaning of galaxy colors with respect to the WISE filter W1. Both characteristics are key inputs into the stellar population models that are used to convert luminosity in the baryonic component that is stellar mass. In addition, the competing Spitzer and WISE photometry data sets provide an opportunity to examine the astrophysics underlying galaxy luminosity at 3.5 μm and the uncertainties in galaxy photometry at these wavelengths for future studies of the distance scale of galaxies (Schombert et al. 2020).

2. Photometry

2.1. The SPARC Galaxy Database

The SPARC data set consists of high-quality H I rotation curves accumulated over the last three decades of radio interferometry combined with deep near-IR photometry from the Spitzer 3.6 μm IRAC camera (Lelli et al. 2016). This

provides the community an important combination of extended H I rotation curves (mapping the galaxy gravitational potential out to large radii) plus near-IR surface photometry to map the stellar component (see also Zaritsky et al. 2014). In addition, the H I observations also provide the H I gas mass that, when corrected for small amounts of He and heavier elements, becomes the total gas mass of a galaxy. The combined stellar and gas components is the total baryonic mass of a galaxy.

The SPARC sample spans a broad range in baryonic mass (10^8–10^{11} $M_\odot$), surface brightness (3–1000 $L_\odot$ pc^{-2}) and rotation velocity (V_f from 20 to 300 km s^{-1}). The SPARC data set also contains every Hubble morphological type from S0 to Irr producing a representative sample of different types of galaxies from dwarf irregulars to massive spirals with large bulges. Details of this sample are listed in Schombert & McGaugh (2014) and the key science results outlined in McGaugh et al. (2016). The SPARC sample, and analysis with respect to the bTFR, are presented in Lelli et al. (2016). The analysis presented herein follows that paper with respect to error analysis plus small additions and corrections to the data as outlined in Lelli et al. (2019). Our larger goal is to expand our near-IR photometry data sets in preparation of the next generation of the SPARC sample from ongoing HI rotation curves studies. As discussed below, in order to compare WISE versus Spitzer photometry, we have isolated a subset of 111 galaxies from the SPARC sample that follow the quality criterion outlined in Lelli et al. (2019) plus have matching WISE and IRAC images free of contaminating bright stars or neighboring galaxies.

2.2. SPARC Photometry Pipeline

With respect to exploring the stellar mass properties of galaxy with kinematic information, such as a rotation curve, there are two critical aspects to the data reduction process. The first is the assignment of a total stellar mass of the galaxy based on a total luminosity at some wavelength that minimizes the uncertainty in going from luminosity to stellar mass. For stellar population reasons, this is best obtained in the near and mid-IR filters (but not so long in wavelength to encounter star-forming hot-dust features in the far-IR; Brown et al. 2014). This is primarily the domain of space imaging with its low IR background. In comparison, UV and optical wavelengths suffer from the short-lived effects of star formation and produce highly color-dependent, and increasingly uncertain, estimates of the mass-to-light ratios (Taylor et al. 2011).

A second data reduction goal is the determination of stellar mass surface density as a function of radius for a point-by-point comparison between baryon mass and the observed rotation curve at that radius (the so-called radial acceleration relation; Lelli et al. 2017). This is the technique of surface photometry (Okamura 1988), the determination of luminosity density along some isophotal shape. The shape of choice is an ellipse, motivated by the empirical observation that ellipses are remarkably good describers of even the most irregular shaped galaxy (Schombert et al. 1992).

The two forms of galaxy photometry, total and isophotal, are coupled as one uses the ellipses defined by a galaxy's surface photometry to determine an isophotal magnitude and an extrapolation of those same ellipses can result in a curve of growth to determine a total luminosity (Schombert 2011). In addition, other scale parameters, such as disk/bulge scale lengths and half-light radii, are also extracted from the surface photometry to quantify galaxy structure and mean density parameters, such as central surface brightness.

While the field of galaxy photometry has a long history (Peletier 2013), there are two primary complications to obtaining accurate surface photometry (and isophotal magnitudes) worthy of particular attention. The first is the problem of a low signal-to-noise ratio (S/N) with respect to the background. Even the brightest galaxies fade to background level at their edges. Depending on a galaxy's light profile, galaxies can have a significant amount of their flux in large, low-S/N apertures. The determination of an accurate total luminosity will require capturing or estimating that flux. The second complication is the contamination of a galaxy's luminosity by foreground stars and nearby galaxy envelopes. This is a particular problem in the IR as the number of point sources are factors of ten higher than in the optical (Schombert & McGaugh 2014; Jarrett et al. 2019). Various photometry programs have dealt with this issue using different techniques ranging from doing nothing to masking point sources to removing point sources with a point-spread function (PSF) algorithm (see early work by Jarrett et al. 2000 and a comprehensive attack on this problem by the GAMA project; Wright et al. 2010).

Various galaxy photometry packages exist for the community (see Muñoz-Mateos et al. 2015 for a detailed description of Spitzer galaxy photometry and Trujillo et al. 2020 for precision analysis of galaxy sizes). Their outputs differ depending on science goals but typically all have a common objective of parameterizing either the total luminosity or some fraction of the total luminosity that can be scaled by morphological type (Sandage & Perelmuter 1990). The photometry for this project used an expanded version of the ARCHANGEL galaxy analysis package (Schombert 2011; Schombert & McGaugh 2014). The ARCHANGEL package was originally designed to analyze optical images of low-surface-brightness galaxies (Schombert et al. 1992), but has many features that are well suited to near-IR imaging, such as special algorithms adjusted for irregular galaxy morphology and low S/N with respect to the sky. Key to the ARCHANGEL package is a fast least-squares ellipse fitting procedure that simultaneously fits and cleans isophotal regions. Cleaning is accomplished by two procedures; (1) a manual masking of deeply embedded stellar sources within the galaxy itself and (2) automatic masking of stars and artifacts in the outer regions by a threshold algorithm. Masked regions are replaced by averaged values from the fitted ellipses for aperture photometry, but left masked for surface photometry evaluation (which uses a mean isophotal value rather than a total flux).

While masking is optimal for smooth, regular galaxies, such as ellipticals, it becomes problematic for highly irregular late-type system with strong star formation which produce clumps and knots that are hard to distinguish from foreground stars (see Figure 2 of Schombert & McGaugh 2014). Surface brightness profiles are extracted from the mean intensities around each fitted ellipse minus the masked regions. Inhibitors to the pipeline prevent sharp changes in ellipse position angle, isophote center and eccentricity which enhances an accurate transition from bulge to disk in early-type disks. If a set error threshold is exceeded, the previous fitted ellipse is used as a default. At the 1% sky threshold fitting is halted, but ellipses are continued to be evaluated to the edge of the frame. These outer ellipses can be compared to sky values obtained by

histogram analysis or sky boxes and provide a direct comparison of the uncertainty in the true sky value.

On the assumption that all of the rotating galaxies in our sample are oblate disks, the semimajor axis is used as the profile radius. Error bars are assigned based on two uncertainties, the standard deviation in pixel intensities around the ellipse and the error in the sky value. For inner isophotes, the standard deviation dominates the error budget. For outer isophotes, the knowledge of the correct background intensity dominates the error, which includes a combination of the flatness of the images as well as the standard deviation on the mean of the sky boxes. For space imaging, frame flatness is rarely a problem and these sky values are also compared with Gaussian fits to the border pixel values (i.e., a histogram sky value). Error bars are assigned through a quadrature average of all the possible errors.

Most photometry projects assign a total magnitude using the Kron system, or some isophotal equivalent (Kron 1980). This technique determines a luminosity weighted radius to define an elliptical aperture where the total flux is summed (see for example an analysis of the SDSS Petrosian magnitudes; Schombert 2016). Often a masking routine has removed non-galaxy pixels from inside the aperture; some techniques replace them with nearby intensity values, others just leave them to be ignored. Depending on the steepness of the galaxy's luminosity profile, a Kron magnitude will capture between 85% and 95% of the total luminosity (Bertin & Arnouts 1996; Schombert 2016), which is similar to the Holmberg magnitude outlined in Schombert (2018). A more detailed treatment of how a galaxy's luminosity profile relates to its total luminosity can be found in Graham & Driver (2005).

The photometric technique for this study also evaluates isophotal magnitudes, but primarily uses curves of growth to determine total luminosities (Schombert & McGaugh 2014). In addition, metric apertures are used for comparison of colors (apertures of a set arcsec size) and surface brightness profiles are used for radial mass profiles. Metric magnitudes are generated by selecting an isophotal radius and summing the pixel fluxes inside that elliptical aperture. However, an isophotal magnitude has variable meaning and does not typically result in an accurate total flux even with aperture corrections (see below). Curves of growth are constructed using the cleaned images and the surface photometry fits. Our procedure differs slightly from raw curves of growth (where one simply sums the flux in each aperture) by using a partial pixel routine on the repaired images (masked pixels replaced with ellipse intensities), and the outer apertures have their fluxes calculated using both the raw pixel values and a mean annular flux defined by the surface brightness at that radius. This has the advantage of suppressing contamination from the wings of bright stars and unmasked faint stars, while simultaneously offering a measure of the photometric uncertainty in the total luminosity by comparison of the raw and corrected aperture values.

Colors are determined through matched apertures, although this is very problematic at small radii when comparing WISE filters to either ground-based optical or Spitzer with their comparatively higher spatial resolution and superior PSF. The rich stellar fields at near-IR wavelengths make aperture to aperture comparison of WISE images to other bandpasses difficult due contamination from the broad PSF wings of foreground stars. Extreme care is required to remove stellar contamination while not reducing significant signal from the galaxy profile. The use of matching metric apertures at least offers some level of control of contaminating stars at large radii. For small apertures, the poor PSF in the WISE images makes aperture to aperture comparisons impossible due to scattered light.

2.3. The WISE and Spitzer Filter Systems

WISE is a NASA 40 cm IR space telescope launched into Sun-synchronous polar orbit in 2009. Its primary mission was to survey the sky at the mid-infrared bands of 3.4, 4.6, 12 and 22 μm (Wright et al. 2010). Our study is focused on the determination of the total baryonic mass of a galaxy and, thus, WISE provides the IR photometry needed to equate luminosity to stellar mass through the use of appropriate mass-to-light ratio (Υ_*; see Cluver et al. 2014 and Kettlety et al. 2018). The filter of choice is 3.4 μm (W1) which uses a HAWAII 1-RG 1024×1024 HgCdTe array with a pixel scale of $2\farcs75$ pixel^{-1} producing a $47' \times 47'$ field of view. WISE images were extracted from NASA/IPAC infrared science archive (IRSA) using the ALLWISE release. Subimages corresponding to 5 times the optical Holmberg radius were always adequate to insure sufficient surrounding blank sky for background determination. Rebinning by ALLWISE resulting in a $1\farcs375$ pixel^{-1} plate scale, with a slight improvement on the PSF.

In comparison, the Spitzer Space Telescope was a 85 cm Ritchey–Chretien launched into an Earth-trailing orbit in 2003 (Werner et al. 2004). The primary imaging instrument is the Infrared Array Camera (IRAC) which used an indium antimonide 256×256 detector. IRAC images were also obtained from IRSA using the Enhanced Image archive. Subimages varied on the field of view, but all had a plate scale of $0\farcs6$ pixel^{-1} through channel 1 of the IRAC camera (hereafter, IRAC 3.6).

A comparison of the W1 and IRAC 3.6 response curves are shown in Figure 1. While the midpoints for W1 and IRAC 3.6 are listed as 3.37 and 3.55 μm, the filters are broad (from 2.8 to 3.9 μm) with the W1 filter having a steeper slope to the blue side. The overlap region covers 73% of the W1 response and 87% of the IRAC 3.6 flux. Notably, both filters cover the PAH feature at 3.3 μm, an emission line associated with young AGB stars and loosely correlated with ongoing star formation (see Meidt et al. 2012; Brown et al. 2014; Querejeta et al. 2015). Due to the high overlap, the W1-3.6 color is expected to be near zero in the AB system. However, there is a slight, but important color term that reflects underlying astrophysics.

Shown in Figure 1 are two averaged spectral energy distributions (SEDs) from the Brown et al. (2014) sample. Our choice of the Brown et al. (2014) data set is one of convenience as we have used this data set in our earlier Spitzer studies. While more recent SED studies are available (see Clark et al. 2018), the Brown et al. SED's are accurate over the wavelengths of interest herein. An average of a dozen galaxies with colors bluer than the mean W1-3.6 (see below) are shown in blue. For comparison, an average with redder than mean colors are shown in red. As discussed in the next section, the bluer W1-3.6 galaxies are typically early-type in morphology, redder are late-type. The steeper SED reflects a stronger bulge component, which dominated the IRS spectra. Galaxies with strong star formation will have a flatter SED with a stronger PAH 3.3 μm feature. The difference in colors can be seen as the

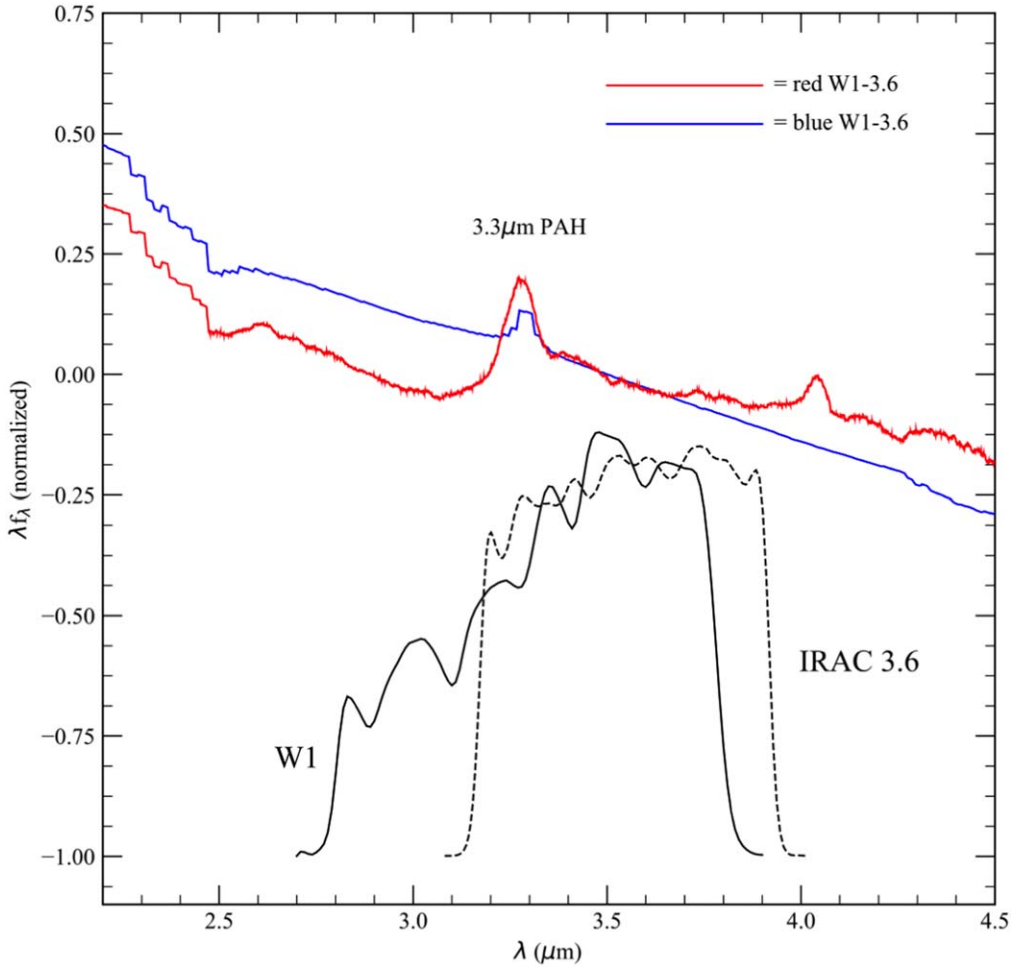

Figure 1. The WISE W1 and Spitzer IRAC 3.6 filter responses in comparison to two different mid-IR SED's from Brown et al. (2014). Note that W1 and IRAC 3.6 have nearly identical wavelength coverage where 73% of the W1 flux matches 87% of IRAC 3.6. W1 samples its remaining flux to the blue of IRAC 3.6, and IRAC 3.6 samples its remaining flux redward of 3.8 μm. Passive galaxies have steep SED's (shown as blue) resulting in blue W1-3.6 colors. Star-forming galaxies have flat SED's resulting in red W1-3.6 colors (opposite to the traditional expectation for galaxy colors). Both filters encompass the 3.3 μm PAH feature associated with AGB stars.

effect of a slightly longer red side for IRAC 3.6 (13% outside the W1 band) and the wider blue wing to W1 (27% shortward of the IRAC 3.6 band). Notice this results in a reverse expectation for typical astronomical colors in that star-forming galaxies will have redder W1-3.6 colors compared to quiescent galaxies with older stellar populations.

It is also important to notice that a hot-dust component due to increased star formation only begins to be significant beyond 4–5 μm. While the 3.3 μm PAH feature increases with star formation, this is balanced in the W1 filter by a relative decrease on the blue side of 3.3 μm. Thus, starlight dominates the flux through both W1 and IRAC 3.6 and stellar mass estimates using these filters will only have slight color component in the direction of higher Υ_* values for older stellar populations (i.e., early galaxy types; see Schombert et al. 2022). In addition, the increased blue sensitivity to W1 compensates for stronger PAH emission to produce a W1 luminosity conversion to stellar mass with much less distortion due to star formation and AGB effects (Schombert & McGaugh 2014). However, a detailed incorporation of an enhanced AGB contribution, as a component of a galaxy's SED at 3.6 μm, is missing from most stellar population models in the literature (see Conroy & Gunn 2010) and we continue to use the empirical correction as a function of metallicity from *K* to 3.6 as given by Schombert et al. (2019).

2.4. Comparison to WISE and Spitzer Photometry in the Literature

One of the earliest near-IR space galaxy photometry projects was the Spitzer Nearby Galaxies Survey (SINGS; Kennicutt et al. 2003). The 3.6 μm photometry was presented in Dale et al. (2007) and used an optically determined elliptical aperture. An additional extended source aperture correction was applied to account for scattered light, typically in the 8%–9% range. There were 12 galaxies in common from the SINGS sample to the SPARC sample, and the resulting $m_{3.6}$ values (in the Vega system) are shown in Figure 2. Two comparisons with the SPARC photometry are shown, the left panel displays the isophotal magnitude from our photometry pipeline that measures the luminosity inside an elliptical aperture defined by the 23 mag arcsec^{-2} isophote (this value is selected as it roughly corresponds to the Holmberg radius of 26.5 *B* mag arcsec^{-2} for the color of late-type galaxies). The right panel displays the 3.6 μm asymptotic magnitude determined from curves of growth described above.

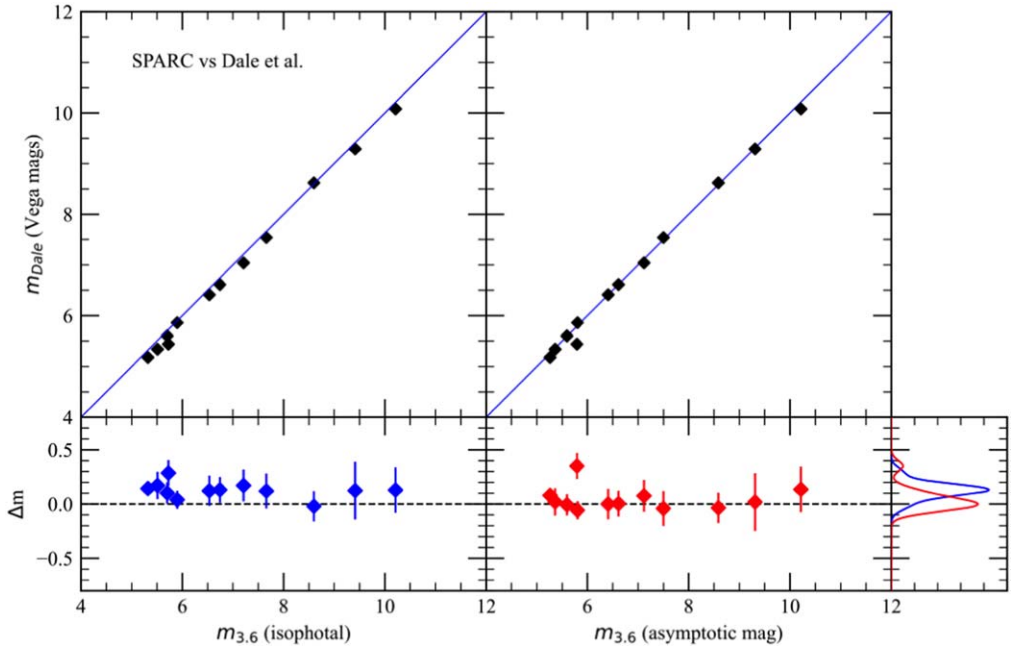

Figure 2. A comparison between the Dale et al. (2007) IRAC 3.6 photometry of the SINGS sample with the SPARC pipeline. There were 12 galaxies in common, the Dale et al. 3.6 μm magnitudes are shown in comparison with SPARC isophotal magnitudes (measured inside an elliptical aperture defined by the 23 3.6 mag arcsec^{-2} isophote) and the asymptotic magnitude determined from curves of growth. The blue line represents unity between the magnitude systems, the correspondence is excellent. The residuals are shown in the bottom panels with a normalized histogram for each panel to the far right.

In general, the correspondence is excellent. The differences between the Dale et al. (2007) luminosities and SPARC are less for the asymptotic magnitudes, but the shift is minor (less than 0.05 mag). The aperture correction procedure for Dale et al. (2007) seems to recover all the missing outer flux and is in good agreement with SPARC's determination of a total luminosity by curves of growth. The typical internal error is quoted as 0.01 by Dale et al. (2007) but the dispersion with respect to the SPARC asymptotic magnitudes is on the order of 0.05 mag.

The most extensive Spitzer galaxy photometry survey is the S^{4}G project (Sheth et al. 2010), which observed 2331 galaxies. The techniques used by the S^{4}G pipeline are very similar to the ARCHANGEL system used by the SPARC pipeline. Background determination used sky boxes and elliptical apertures are defined by the outer isophotes of the target galaxy. Total luminosities are assigned by fitting the accumulated magnitude as a function of the magnitude gradient to obtain an asymptotic magnitude. The only minor difference between SPARC and S^{4}G pipelines is the lack of replacement of masked pixels with a nearby mean intensity, which typically results in a systematic shift of 5% for Spitzer elliptical samples (see Schombert & McGaugh 2014).

There were 51 galaxies in common with SPARC and S^{4}G samples, their comparison is shown in Figure 3. While the correspondence is one to one, the S^{4}G luminosities were 10% fainter than our asymptotic magnitudes and 7% fainter than our isophotal magnitudes. This does not reflect uncertainties in the photometry but rather the different techniques used to determine a total luminosity. Most of the difference is found at the faint magnitudes where our procedure of replacing masked pixels with mean galaxy surface brightness produces a notable increase in total galaxy luminosity compared to the brighter galaxies. This also serves as a cautionary tale considering the error budget for galaxy photometry is often quoted at the 1% level, but clearly the technique and isophote chosen can lead to 10% differences in various determinations of a total stellar mass. The dispersion around the offset magnitude is on the order of 0.08 mag.

With respect to WISE W1 photometry, one of the earliest papers to use WISE photometry for analyzing the Tully–Fisher relation is Neill et al. (2014). Using WISE W1 and W2 photometry on 310 galaxies in 13 clusters, they explore the absolute magnitude to H I line width relationship. As with the S^{4}G project, their photometry pipeline is similar to SPARC using drizzled WISE images extracted from IRSA. Total luminosities are defined from an asymptotic magnitude that is the integration of the galaxy radial profile.

The SPARC and Neill et al. samples have 28 galaxies in common, shown in Figure 4. The agreement is excellent with a slight tendency for the SPARC isophotal W1 values to underestimate the Neill et al. asymptotic magnitudes at faint luminosities (roughly 5% below $m_{W1} = 10$). The comparison to Spitzer 3.6 μm asymptotic is also strong with a mean offset of 0.1 mag in concurrence with the average W1-3.6 color term. Again, the mean internal photometry error at W1 is similar to 3.6 at the 0.01 mag level, although the dispersion is on order of 0.1 mag.

Two other recent surveys of the WISE images related to the Tully–Fisher relation are Cluver et al. (2014) and Bell et al. (2023). Both studies follow the procedure pioneered in Jarrett et al. (2013), which is nearly identical to the SPARC photometry pipeline in using elliptical apertures with curves of growth combined with replacing masked pixels with local intensity values. These studies have 17 galaxies in common with the SPARC WISE sample and are shown in Figure 5. As before, the agreement is excellent with a dispersion of only 0.08 mag. While this is higher than the quoted errors in all the photometry pipelines, it more accurately reflects the limit to repeatability in galaxy photometry. The Spitzer asymptotic

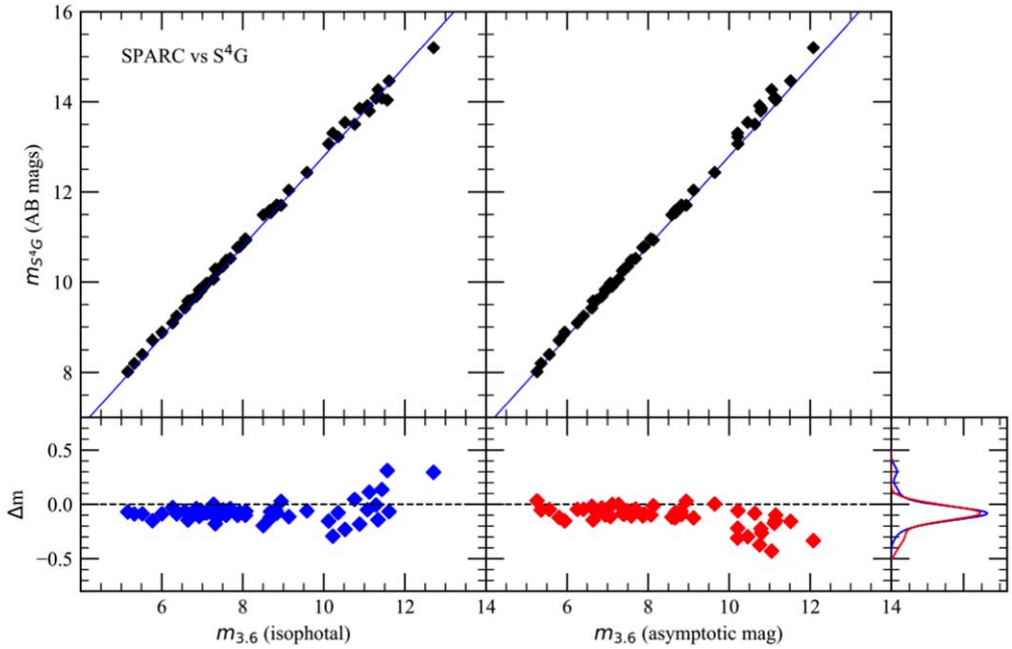

Figure 3. A comparison between the S^{4}G IRAC 3.6 photometry (Sheth et al. 2010) with the SPARC pipeline. There were 51 galaxies in common, the correspondence is good with a 7%–10% shift between SPARC and S^{4}G fluxes with either isophotal apertures or asymptotic magnitudes. The residuals are shown in the bottom panels with a normalized histogram for each panel to the far right. We attribute the difference to varying photometric techniques (see text).

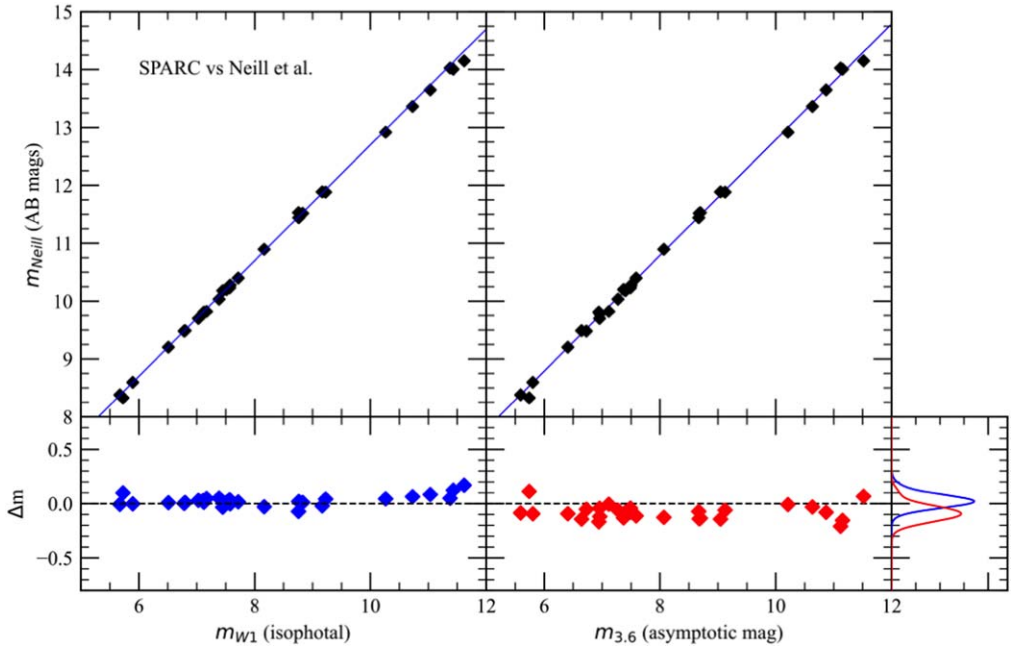

Figure 4. A comparison between the Neill et al. (2014) WISE photometry and SPARC WISE. Both SPARC and Neill et al. use similar photometric pipelines, particularly with respect to the use of drizzled WISE images. The residuals are shown in the bottom panels with a normalized histogram for each panel to the far right. The correspondence is excellent with a slight deviate at low luminosities. The comparison with asymptotic 3.6 mag recovers this missing flux.

magnitudes display the same correspondence with a color offset of 0.2 mag.

Lastly, we compare our pipeline results with two spectro-photometric surveys, from Brown et al. (2014) and Vaddi et al. (2016). The comparison with Brown et al. (2014) is particular salient as that study was a comprehensive analysis of the SEDs of 129 galaxies from the UV to the mid-IR for varying morphological types and a range of current SFR's. There were 34 galaxies in common with an ongoing extension of the SPARC sample (SPARC 1k) and comparison is shown in the left panel of Figure 6. The focus of Brown et al. was to match standard filter flux to the deep optical and IR spectra for the same galaxies. This resulted in different apertures for their W1 and 3.6 μm luminosities, which would seem to explain the large scatter in Figure 6. We note that the offset goes to zero if we assume the Brown et al. fluxes are based on a Kron magnitude definition (i.e., 90% the total flux, shown by the dotted line in Figure 6), but the dispersion is still larger than accountable by pure photometric errors. Also shown are the aperture magnitudes from the DustPedia survey (Clark et al.

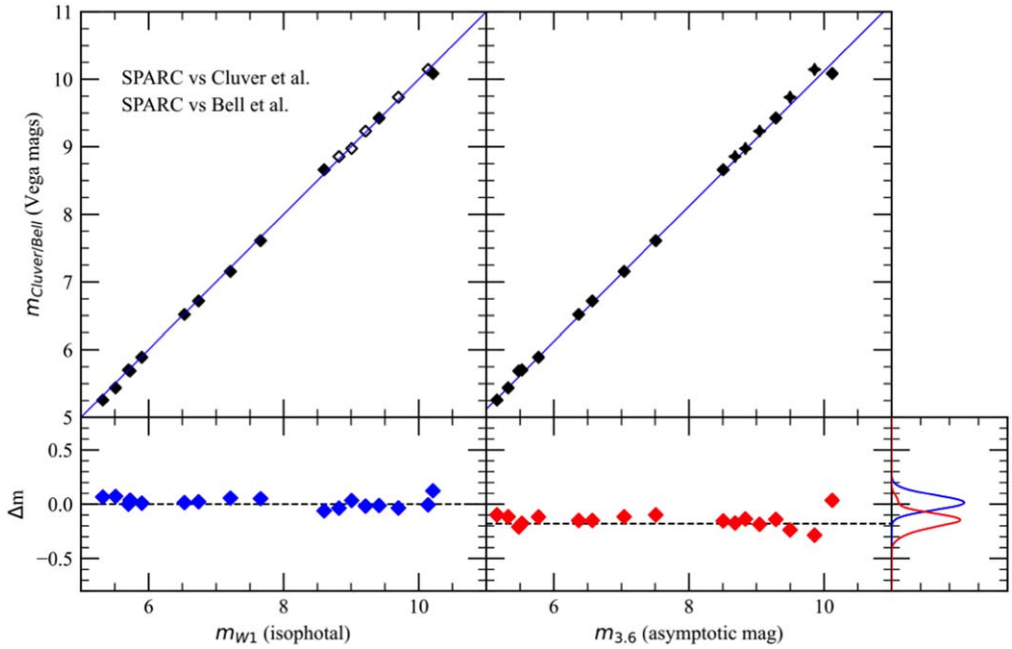

Figure 5. A comparison with the W1 and IRAC 3.6 photometry of Cluver et al. (2014) and Bell et al. (2023). The residuals are shown in the bottom panels with a normalized histogram for each panel to the far right. Both these studies use the procedures developed in Jarrett et al. (2013) and there is an excellent correspondence over five orders of magnitude.

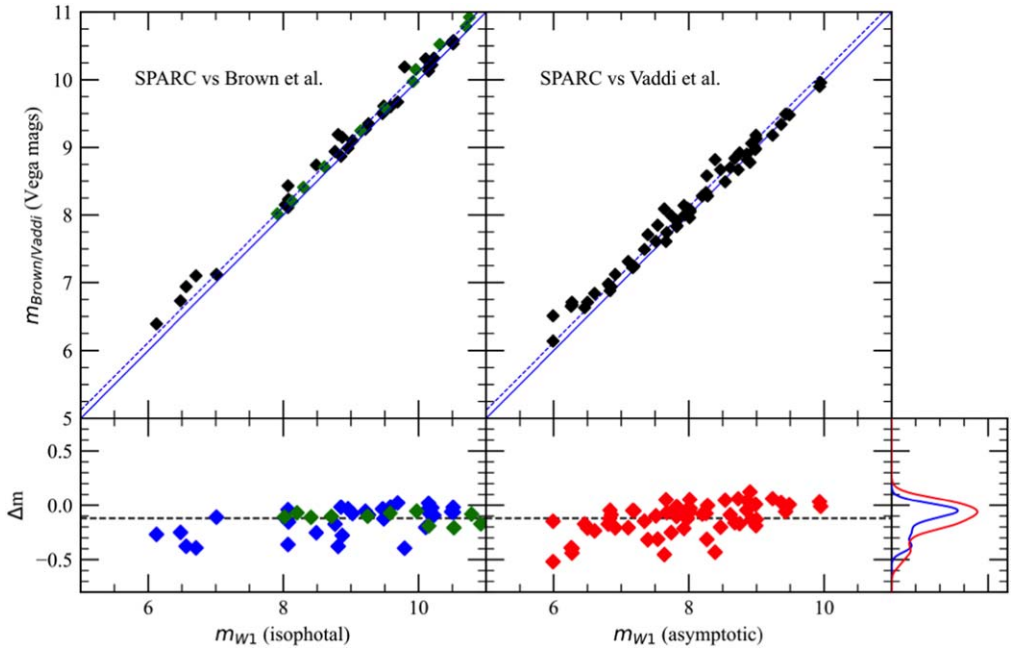

Figure 6. A comparison with the SED study of Brown et al. (2014), Clark et al. (2018), and WISE photometry from Vaddi et al. (2016). The residuals are shown in the bottom panels with a normalized histogram for each panel to the far right. The correspondence is good, but the dispersion is higher than previous comparisons. For the Brown et al. (2014; black symbols) and Clark et al. (2018; green symbols) studies, this reflects varying aperture sizes that appear to reproduce a Kron magnitude (90% the total luminosity shown by the dashed line). The Vaddi et al. (2016) also has a larger dispersion, but with the largest overlap to the SPARC sample in terms of galaxy numbers. The dashed line is the 90% flux comparison. The dispersion from this offset is 0.06 mag, which probably reflects the true uncertainty in galaxy photometry regardless of error bars quotes by each study.

2018), a similar SED study from the UV to far-IR with 11 galaxies in common with our SPARC sample.

The data from Vaddi et al. had 61 galaxies in common with the new SPARC 1k sample. Vaddi et al. use an isophotal defined aperture where the aperture size is given as one standard deviation above mean sky value. Foreground stars are masked, but missing flux is not replaced. Again, as seen in the right panel of Figure 6, the dispersion is higher than other samples, and the SPARC sample are typically 5%–10% brighter than the Vaddi et al. fluxes. Again, we interpret this difference as due to technique differences rather than errors in the photometry.

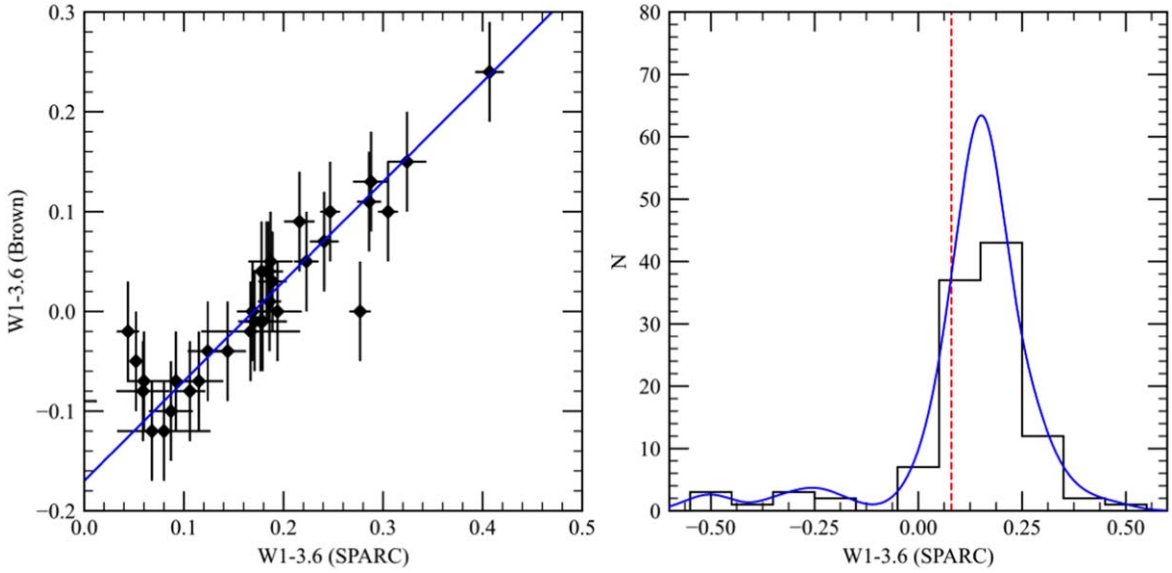

Figure 7. The left panel displays a comparison of aperture colors between SPARC and Brown et al. (2014). The relationship is one-to-one in relative values, and the dispersion is within the observational errors (a mean error bar is shown). However, there is a 0.17 mag shift from the Brown et al. W1-3.6 colors compared to SPARC. We attribute this to differences in the zero point of the AB system used by Brown et al. and varying aperture sizes between their WISE and Spitzer measurements. The right panel displays a histogram of SPARC W1-3.6 colors. We note that a majority are redward of the mean elliptical color (red dashed line; Schombert 2016), in agreement with the expectation that star-forming disks will have redder colors than passive, old stellar population galaxies.

2.5. W1 to IRAC 3.6 Colors

The WISE to Spitzer color sequence is poorly explored in the literature. This is primarily due to the fact that since W1 and IRAC 3.6 are so similar in their wavelength response, the two fluxes are nearly identical and there was limited information in their ratios with respect to star formation history. However, there is a clear distinction between blue and red W1-3.6 values with respect to the Brown et al. (2014) SEDs. The slight blue and red wings to the W1 and IRAC 3.6 filters maps well into the two distinct SED shapes for galaxies: (1) power-law shaped SED and (2) ones with flat flux around the 3.3 μm PAH feature. In particular, we found in Section 2 that steep SEDs are associated with blue W1-3.6 colors and flat SEDs are aligned with red W1-3.6 colors. However, the difference between the blue and red SEDs in Figure 1 is only 10% of the total W1 flux, which corresponds to a small shift of 0.2 mag in the AB system.

There are few studies in the literature with matching WISE and Spitzer apertures to compare colors. The Brown et al. (2014) sample provided adjusted W1 and IRAC 3.6 fluxes for comparison to SPARC W1-3.6 colors. This comparison is shown in Figure 7. The correspondence is good except for a 0.17 mag shift due to a calibration shift from AB to Vega magnitudes plus a mismatch between the WISE and IRAC 3.6 apertures in the Brown et al. sample. However, the dispersion from a line of unity matches the typical photometric errors in each filter, giving some confidence that both techniques are measuring the same flux difference, i.e., the external color errors are in the range of 0.04–0.06 mag.

A subsample of the SPARC sample was selected for color analysis where each galaxy was without contaminating bright stars near the isophotal aperture. This resulted in 111 galaxies with good W1-3.6 values shown as a histogram in Figure 7. The mean W1-3.6 color of a L^* elliptical is shown as the red line (Schombert 2018). The SPARC sample primarily falls in the red side of W1-3.6 colors, which we have seen in the previous section associates with SED's dominated by recent star formation. This agrees with the fact that SPARC focuses on a sample of primarily spirals and dwarfs irregulars with varying amounts of ongoing star formation. The early-type galaxies, with prominent bulges, occupy the blue side of the histogram. Galaxies with Seyfert or LINER signatures have the bluest W1-3.6 colors (see the next section).

3. The WISE SPARC Sample

A subset of 111 galaxies were selected from the 175 galaxies in the original SPARC sample. The subset was chosen for good image quality in both WISE and Spitzer frames, meaning a well-defined galaxy profile with no nearby bright stars or bright galaxies. In order to ensure that resolution differences between WISE and Spitzer did not bias the aperture magnitudes, we placed a 30″ radius limit to the metric apertures.

The SDSS, WISE and Spitzer magnitudes are listed in Table 1, where the aperture used was the ellipse from Spitzer surface photometry interpolated to the 23 3.6 μm mag arcsec^{-2} isophote. In addition to WISE and Spitzer photometry, the SDSS archive was searched for SDSS g and r images for the same galaxies. Of the WISE sample, 79 were found in the SDSS archive. The same metric aperture was applied to the SDSS images.

Errors were assigned from two characteristics of the images. The first is standard Poisson noise from the galaxy flux itself. All the galaxies were significantly larger than either the Spitzer or WISE PSFs, so the areal flux was converted back into photon counts for a $\sqrt{N}$ determination. The Poisson error was always a factor of ten smaller than the error due to the background noise. The error in the sky value was assigned through the use of sky boxes. Typically over ten boxes of 20 by 20 pixels were selected from regions at the edge of the frames devoid of stars or faint galaxies. The pixels in each box were averaged with a jack-knife procedure and the dispersion of the mean of those boxes is assigned as the error on the sky value. The area of the aperture is multiplied by sky error and added in

Table 1
SPARC Photometry

Name	R (arcsec)	m_g	m_r	m_{W1}	$m_{3.6}$
F568-1	28.3	16.173 ± 0.102	⋯	13.864 ± 0.153	13.675 ± 0.148
F568-3	42.5	15.826 ± 0.107	15.411 ± 0.092	13.376 ± 0.072	13.093 ± 0.114
F568-V1	21.1	16.705 ± 0.114	16.345 ± 0.097	14.192 ± 0.091	13.855 ± 0.123
F571-V1	15.6	17.680 ± 0.160	17.288 ± 0.149	15.152 ± 0.130	14.915 ± 0.196
F574-1	30.2	16.777 ± 0.096	16.333 ± 0.073	14.014 ± 0.066	13.613 ± 0.114

Note. Only the first five galaxies are shown. The rest are in the electronic version.
(This table is available in its entirety in machine-readable form.)

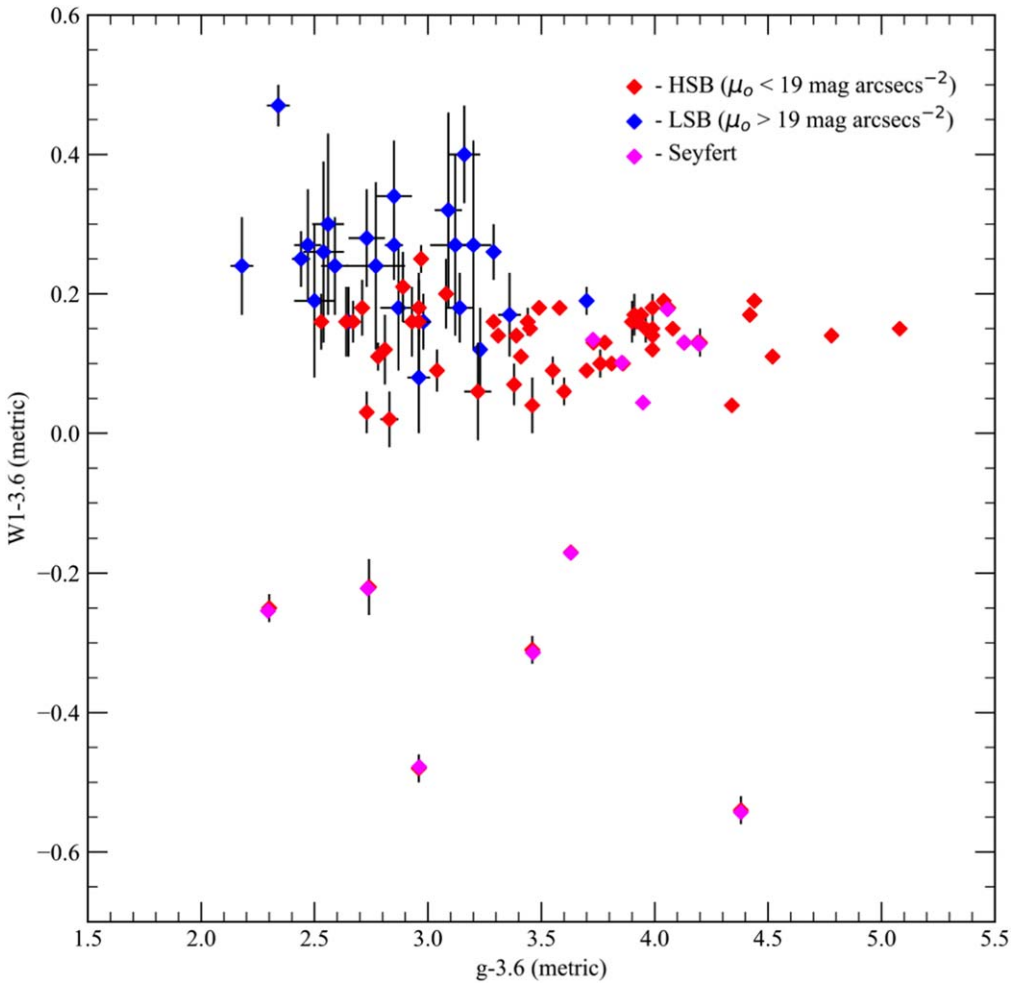

Figure 8. The optical g-3.6 color compared to the IR W1-3.6 color for 87 galaxies in the SPARC sample with both WISE and SDSS imaging. While there is a wide dispersion in optical color, the range in W1-3.6 color is quite small (when Seyferts are excluded). The distinction between LSB and HSB galaxies in W1-3.6 probably reflects a metallicity effect (see Figure 10).

quadrature with the Poisson error for the final uncertainty in magnitude listed in Table 1.

The resulting g-3.6 versus W1-3.6 two-color diagram from Table 1 is shown in Figure 8. The g-3.6 color is similar to V-3.6 used in our previous star formation history studies (Schombert et al. 2019) and covers the full range in color found for spirals and irregulars noted in larger galaxy catalogs. In particular, V-3.6 is the benchmark color for assigning a mass-to-light ratio (Υ_*) value from stellar population models (see Figure 2 of Schombert et al. 2022).

The general characteristics of the two-color diagram followed those found for the K-3.6 diagram (Schombert & McGaugh 2014). There is a slight redward slope, which we now understand as due to flatter SED's at 3.6 μm for star-forming, optically blue galaxies. There are several galaxies with W1-3.6 values below zero that signal steep SED's associated with quiescent stellar populations. However, we note that all the very blue W1-3.6 galaxies (W1-3.6 less than 0) also show Seyfert or LINER signatures in their optical spectra. Seyferts lack the 3.3 μm PAH feature in the Brown et al. (2014) SEDs combined with much steeper blue-side fluxes in the W1

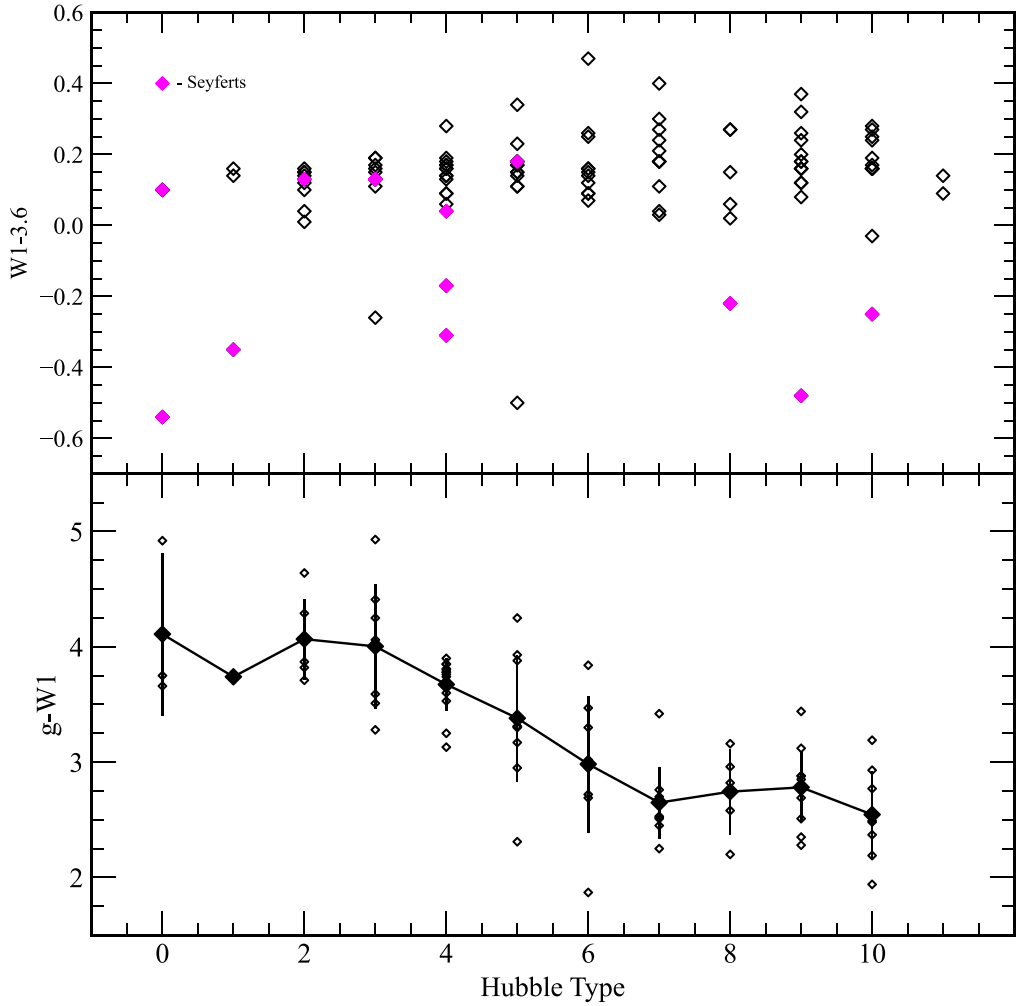

Figure 9. The range in optical and IR color with respect to Hubble type for the SPARC sample. The trend in g-W1 matches the known trends outlined in Schombert & McGaugh (2021). The slight trend for redder W1-3.6 color with later Hubble type is not statistically significant and demonstrates why IR fluxes are significantly better for stellar mass determinations than optical flux due to their independence from star formation history as related to galaxy type.

filter. This nonthermal component would explain the extreme W1-3.6 colors.

We also note the unusual color signature displayed by low-surface-brightness (LSB) galaxies. If the SPARC sample is divided in high and low central surface brightness (defined in Schombert & McGaugh 2014), then a clear color distinction is displayed such that LSB galaxies have redder W1-3.6 colors on average (also bluer g-3.6 colors, which was well known from early LSB studies; Pildis et al. 1997). Unusual colors for LSB disks is usually interpreted as a signature of low metallicities (Schombert & McGaugh 2021) and lower metallicity does drive up the red side of the IRAC 3.6 filter, based on K-3.6 colors and stellar population models (see Schombert et al. 2022).

The distinction between LSB and HSB galaxies in W1-3.6 color can be seen in the stellar population models of Schombert et al. (2019), where the steady decline in Υ_* levels off at g-3.6 colors less than 3. The increased flux in the IRAC 3.6 filter balances what would normally be the mass-to-light ratios at those wavelengths. Interestingly, the sample of HSB galaxies, with Seyfert objects removed, have a nearly constant W1-3.6 color of 0.14 ± 0.05.

The meaning of the W1 and IRAC 3.6 colors is clearer when we compare W1-3.6 and the SDSS g-3.6 colors as a function of Hubble type (shown in Figure 9). The correlation of bluer optical colors with later Hubble types is clear, the colors closely correspond to the V-3.6 colors from Schombert et al. (2019). In fact, as argued in Schombert et al. (2019), the trend in Hubble type with color also tracks the deduced Υ_* model value such that either color or morphology serves equally well to assign an accurate Υ_* to a particular galaxy. Thus, the clear trend with g-W1 is reassuring as this color is used to define the color-Υ_* relationship from stellar population models.

The trend of W1-3.6 with Hubble type is distinctly different. There is a slight tendency to find redder W1-3.6 colors with later Hubble types, but a least-squares fit is indistinguishable from a zero slope line. The dispersion in color is similar for each category from g-W1 to W1-3.6. Again, we note extremely blue W1-3.6 galaxies have Seyfert signatures. We expect the stellar mass values assigned from either W1 or IRAC 3.6 fluxes will produce similar values, unless the galaxy in question displays AGN activity.

Lastly, the most common color correlation with respect to galaxies is the color–magnitude relation (CMR), usually interpreted to be an age/metallicity correlation between galaxy mass and color (see Sextl et al. 2023 for a recent review). Figure 10 displays the optical and IR CMR with respect to absolute 3.6 μm luminosity. The correlation with optical g-W1

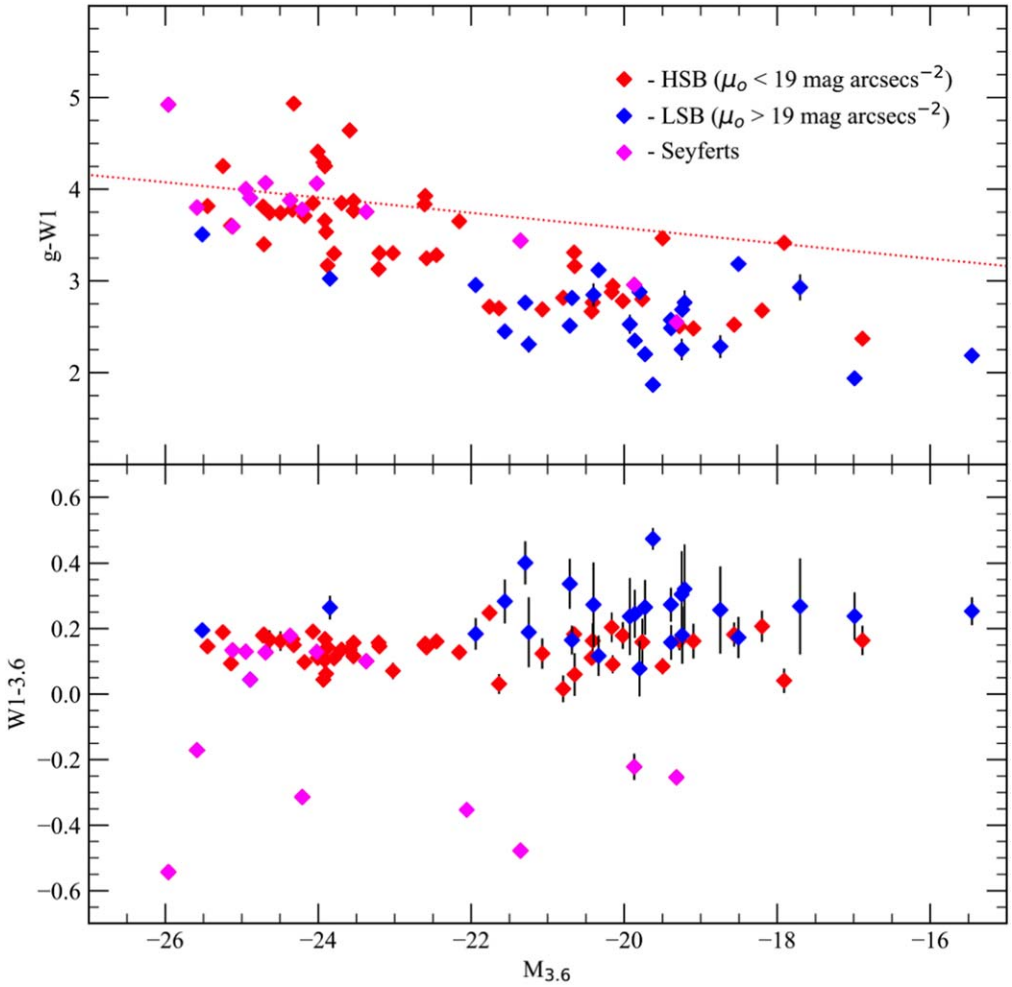

Figure 10. The near-IR and optical color–magnitude relation for the SPARC sample. The upper panel displays the SDSS *g* vs. WISE W1 color where HSB and LSB are marked as red and blue respectively. Seyferts or LINER galaxies are colored magenta. The CMR for ellipticals are indicated by the red dotted line (Schombert 2018). The difference between the passive ellipticals and spirals/dwarfs of the SPARC sample is evident in the steeper, bluer colors due to recent star formation. The dispersion in the elliptical CMR is very small at 0.1 mag whereas the large scatter in the SPARC galaxies represents a wide range in star formation histories as well as slower chemical enrichment. The lower panel displays the CMR for the near-IR color W1-3.6 where star formation effects are negligible. Aside from the Seyfert outliers, the range in W1-3.6 color is small and constant over the luminosity range of the SPARC sample.

color is clear and with a scatter typical for late-type galaxies (reflecting varying star formation history paths; Tojeiro et al. 2013). The dotted line displays the CMR for pure ellipticals (Schombert 2018) that track the mass–metallicity relationship for single burst stellar populations.

As shown in Tojeiro et al. (2013), passive galaxies display IR colors proportional to their stellar mass in agreement with a standard chemical enrichment scenario where a greater gravitational potential produces rapid grow in metallicity and redder stellar populations. They also found that early-type spirals, where the galaxy color is dominated by metal-rich bulges, also overlap the elliptical colors. Galaxies with more star formation display bluer *g*-W1 colors and form the so-called "blue cloud" below the elliptical sequence. Galaxies below −22 divide into two groups where lower mean metallicity pushes LSB galaxies to bluer colors than expected from their star formation histories.

The IR W1-3.6 color displays a slight inverse correlation, mostly driven by LSB galaxy colors, that tracks the expectation of metallicity models for low-mass dwarf galaxies. Again, Seyfert galaxies with their steep SED's are indicated and form 80% of the outliers. The consistence in the near-IR colors again demonstrates an important aspect with respect to stellar mass determination in that neither strong star formation nor a wide range in metallicity alter the W1 versus IRAC 3.6 fluxes by a significant amount. Aside from AGN activity, the near-IR fluxes are remarkably stable over a range of galaxy colors and morphological types.

4. Summary

The primary goal of this study was to link the Spitzer and WISE photometry results for the SPARC sample with special attention to the role of near-IR colors for stellar population models that are used to estimate the stellar mass component of a galaxy. We summarize are main results as the following:

1. The photometry pipeline used for this, and future, SPARC projects focuses on the use of asymptotic magnitudes for total luminosities and metric apertures for colors. Notable differences between Spitzer and WISE photometric values were found to be due to the much poorer PSF for the ALLWISE archive compared to Spitzer.

2. A comparison of several WISE W1 and IRAC 3.6 data sets confirms that differing photometry techniques results in variations of up to 10% for galaxies in common. When comparing with studies that use identical photometry techniques the differences are at the 0.01 mag level, which probably represents the true error in galaxy total luminosities, rather than the formal errors output from the various pipelines.
3. The W1-3.6 colors display excellent one-to-one correspondence with SED studies (e.g., Brown et al. 2014). Positive W1-3.6 colors are associated with galaxies with significant star formation. Strongly negative W1-3.6 colors are found for Seyfert and LINER galaxies. For non-AGN system, the range in W1-3.6 color is fairly limited and only slighter redder than the mean for elliptical galaxies.
4. The optical to near-IR two-color diagram indicates a notable difference between LSB and HSB galaxies, probably related to mean metallicity differences (i.e., bluer RGB populations) rather than star formation as their *g*-3.6 colors are similar. We found that correcting for central surface brightness will improve the stellar mass estimates by 5%, depending on the suite of stellar population models used.
5. The W1-3.6 color is independent of morphology type, other than the tendency for LSB galaxies to be of late Hubble types, while the optical *g*-W1 color is very sensitive to galaxy type. The distinction will be important in linking WISE to Spitzer stellar mass models in our second paper.
6. The optical and near-IR color–magnitude diagrams display the same blue versus red cloud features noted by earlier studies, particularly the SDSS colors of Tojeiro et al. (2013). The *g*-W1 CMR reproduces all the features of the SPARC *g*-3.6 CMR and, in addition, singles out galaxies with strong AGN features. The near-IR W1-3.6 CMR display almost zero slope, raising our confidence in applying mass-to-light ratios across a range of stellar masses.

Acknowledgments

Software for this project was developed under NASA's AIRS and ADAP Programs. This work is based in part on observations made with the Spitzer Space Telescope, which is operated by the Jet Propulsion Laboratory, California Institute of Technology under a contract with NASA. Support for this work was provided by NASA through an award issued by JPL/Caltech. Other aspects of this work were supported in part by NASA ADAP grant NNX11AF89G and NSF grant AST 0908370. As usual, this research has made use of the NASA/IPAC Extragalactic Database (NED), which is operated by the Jet Propulsion Laboratory, California Institute of Technology, under contract with the National Aeronautics and Space Administration. F.D. wishes to thank the University of Oregon's Presidential Undergraduate Research program which supported the initial stages of this project as her honors thesis.

ORCID iDs

Francis Duey https://orcid.org/0009-0003-1662-5179
James Schombert https://orcid.org/0000-0003-2022-1911
Stacy McGaugh https://orcid.org/0000-0002-9762-0980
Federico Lelli https://orcid.org/0000-0002-9024-9883

References

Bell, R., Said, K., Davis, T., et al. 2023, MNRAS, 519, 102
Bertin, E., & Arnouts, S. 1996, A&AS, 117, 393
Bradford, J. D., Geha, M. C., & Blanton, M. R. 2015, ApJ, 809, 146
Brown, M. J. I., Moustakas, J., Smith, J.-D. T., et al. 2014, ApJS, 212, 18
Clark, C. J. R., Verstocken, S., Bianchi, S., et al. 2018, A&A, 609, A37
Cluver, M. E., Jarrett, T. H., Hopkins, A. M., et al. 2014, ApJ, 782, 90
Conroy, C., & Gunn, J. E., 2010 FSPS: Flexible Stellar Population Synthesis, Astrophysics Source Code Library, ascl:1010.043
Dale, D. A., Gil de Paz, A., Gordon, K. D., et al. 2007, ApJ, 655, 863
Duey, F., Tosi, S., & Schombert, J. 2023, AAS, in press
Freeman, K. C. 1999, The Low Surface Brightness Universe, 170, 3
Graham, A. W., & Driver, S. P. 2005, PASA, 22, 118
Iorio, G., Fraternali, F., Nipoti, C., et al. 2017, MNRAS, 466, 4159
Jarrett, T. H., Chester, T., Cutri, R., et al. 2000, AJ, 119, 2498
Jarrett, T. H., Cluver, M. E., Brown, M. J. I., et al. 2019, ApJS, 245, 25
Jarrett, T. H., Masci, F., Tsai, C. W., et al. 2013, AJ, 145, 6
Kennicutt, R. C., Armus, L., Bendo, G., et al. 2003, PASP, 115, 928
Kettlety, T., Hesling, J., Phillipps, S., et al. 2018, MNRAS, 473, 776
Kourkchi, E., Tully, R. B., Anand, G. S., et al. 2020, ApJ, 896, 3
Kron, G. E. 1980, RA, 10, 3
Lelli, F., McGaugh, S. S., & Schombert, J. M. 2016, AJ, 152, 157
Lelli, F., McGaugh, S. S., Schombert, J. M., et al. 2017, ApJ, 836, 152
Lelli, F., McGaugh, S. S., Schombert, J. M., et al. 2019, MNRAS, 484, 3267
McGaugh, S. S. 2012, AJ, 143, 40
McGaugh, S. S., Lelli, F., & Schombert, J. M. 2016, PhRvL, 117, 201101
McGaugh, S. S., Schombert, J. M., Bothun, G. D., et al. 2000, ApJL, 533, L99
Meidt, S. E., Schinnerer, E., Knapen, J. H., et al. 2012, ApJ, 744, 17
Muñoz-Mateos, J. C., Sheth, K., Regan, M., et al. 2015, ApJS, 219, 3
Neill, J. D., Seibert, M., Tully, R. B., et al. 2014, ApJ, 792, 129
Okamura, S. 1988, PASP, 100, 524
Peletier, R. F. 2013, Secular Evolution of Galaxies (Cambridge: Cambridge Univ. Press), 353
Pildis, R. A., Schombert, J. M., & Eder, A. 1997, ApJ, 481, 157
Querejeta, M., Meidt, S. E., Schinnerer, E., et al. 2015, ApJS, 219, 5
Sakai, S., Mould, J. R., Hughes, S. M. G., et al. 2000, ApJ, 529, 698
Sandage, A., & Perelmuter, J.-M. 1990, ApJ, 350, 481
Schombert, J., 2011 ARCHANGEL: Galaxy Photometry System, Astrophysics Source Code Library, ascl:1107.011
Schombert, J., & McGaugh, S. 2021, AJ, 161, 91
Schombert, J., McGaugh, S., & Lelli, F. 2019, MNRAS, 483, 1496
Schombert, J., McGaugh, S., & Lelli, F. 2020, AJ, 160, 71
Schombert, J., McGaugh, S., & Lelli, F. 2022, AJ, 163, 154
Schombert, J. M. 2016, AJ, 152, 214
Schombert, J. M. 2018, AJ, 155, 69
Schombert, J. M., Bothun, G. D., Schneider, S. E., et al. 1992, AJ, 103, 1107
Schombert, J. M., & McGaugh, S. 2014, PASA, 31, e011
Sextl, E., Kudritzki, R.-P., Zahid, H. J., et al. 2023, ApJ, 949, 60
Sheth, K., Regan, M., Hinz, J. L., et al. 2010, PASP, 122, 1397
Taylor, E. N., Hopkins, A. M., Baldry, I. K., et al. 2011, MNRAS, 418, 1587
Tojeiro, R., Masters, K. L., Richards, J., et al. 2013, MNRAS, 432, 359
Trujillo, I., Chamba, N., & Knapen, J. H. 2020, MNRAS, 493, 87
Tully, R. B., & Fisher, J. R. 1977, A&A, 54, 661
Vaddi, S., O'Dea, C. P., Baum, S. A., et al. 2016, ApJ, 818, 182
Verheijen, M. A. W. 2001, ApJ, 563, 694
Werner, M. W., Roellig, T. L., Low, F. J., et al. 2004, ApJS, 154, 1
Wright, E. L., Eisenhardt, P. R. M., Mainzer, A. K., et al. 2010, AJ, 140, 1868
Zaritsky, D., Courtois, H., Muñoz-Mateos, J.-C., et al. 2014, AJ, 147, 134